

# Atmospheric polarimetric effects on GNSS Radio Occultations: The ROHP-PAZ field campaign

R. Padullés<sup>1</sup>, E. Cardellach<sup>1</sup>, M. de la Torre Juárez<sup>2</sup>, S. Tomás<sup>1</sup>, J. F. Turk<sup>2</sup>,  
S. Oliveras<sup>1</sup>, C. O. Ao<sup>2</sup>, and A. Rius<sup>1</sup>

<sup>1</sup>Institut de Ciències de l'Espai (ICE - CSIC / IEEC), Barcelona, Spain

<sup>2</sup>NASA Jet Propulsion Laboratory, California Institute of Technology, Pasadena, CA, USA

*Correspondence to:* Ramon Padullés (padulles@ice.cat)

**Abstract.** This study describes the first experimental observations showing that hydrometeors induce polarimetric signatures in Global Navigation Satellite System (GNSS) signals. This evidence is relevant to the PAZ Low Earth Orbiter, which will test the concept and applications of polarimetric GNSS Radio Occultation (RO) (i.e. ROs obtained with a two-polarization antenna). A ground  
5 field campaign was carried out in preparation for PAZ to verify the theoretical sensitivity studies about this concept (Cardellach et al., 2015). The main aim of the campaign is to identify and understand the factors that might affect the polarimetric GNSS observables. Studied for the first time, GNSS signals measured with two polarimetric antennas (H, horizontal and V, vertical) are shown to discriminate heavy rain events, by comparing the measured phase difference between the H and V  
10 phase delays ( $\Delta\Phi$ ) in different weather scenarios. The measured phase difference indicates higher dispersion under rain conditions. When individual events are examined, significant increases of  $\Delta\Phi$  occur when the radio signals cross rain cells. Moreover, the amplitude of such signal is much higher than the theoretical prediction for precipitation; thus other sources of polarimetric signatures have been explored and identified. Modelling of other hydrometeors like melting particles and ice crystals  
15 have been proposed to explain the obtained measurements, with good agreement in more than 90% of the cases.

## 1 Introduction

Global Navigation Satellite System (GNSS) Radio Occultations (RO) space-borne missions have been probing the Earth's atmosphere since 1995 (e.g. Rocken et al., 1997). They have been shown  
20 to be useful for climate monitoring (e.g. Steiner et al., 2011) and nowadays their thermodynamic profiles are being assimilated operationally into several numerical weather prediction (NWP) models (e.g. Healy et al., 2005; Cucurull and Derber, 2008).

A new measurement concept presented in Cardellach et al. (2015) aims at detecting and quantifying heavy precipitation events using polarimetric GNSS RO, by means of measuring the difference  
25 between the phase delays of the horizontal and the vertical components of the received propagated

signal. This technique will be tested aboard the PAZ Low Earth Orbiter (LEO) satellite with the RO and Heavy Precipitation experiment (ROHP-PAZ), and it will be the first attempt to detect rain using L band frequencies (1.575 GHz, i.e.  $\lambda = 19.03$  cm). The launch is planned for Q1 2016. The theoretical analysis performed in Cardellach et al. (2015) demonstrated not only that heavy rain events could be detected, but also that an approximated vertical structure of the rain cells could be retrieved.

Prior to the launch of the PAZ satellite, a field campaign has been conducted in order to study, for the first time, L1 co-polarizing signals obtained at two polarizations, and start to identify and understand the factors that might affect the polarimetric signal. Placed on top of a mountain peak 1670 m above the mean sea level, the experiment was set up with an engineering model of the PAZ's polarimetric antenna pointing at the horizon and a commercial JAVAD receiver (provided by the German Research Center for Geosciences GFZ), enclosed in a shelter. A zenith-looking geodetic GNSS antenna has also been used for positioning. The RO antenna points south and to the horizon, and it tracks all the visible satellites in the East-West field of view from 40 degrees of elevation and from 150 to 270 degrees of azimuth (see Fig.1). Although all the satellites are tracked simultaneously, only those crossing the main beam of the antenna are used in the posterior analysis. For the time period analyzed, the GNSS satellites with the highest number of samplings are the ones identified by the Pseudo-Random Noise (PRN) numbers G10, G14, G15, G22 and G31. Also, only the segments between 0 and 20 degrees of elevation are used for the analysis, since the antenna performance reaches its optimal values within this range. Given the geometry of the experiment's field of view, in most of the cases only one of either the descending or ascending trajectories over the horizon provided data within the antenna field of view.

The main objective was to collect a large amount of data free of rain, and to catch some heavy rain events in order to observe differences in the polarimetric observables between the two data sets. The area was chosen specifically for this purpose, given that the region is mainly dry and several intense local Mediterranean storms occur a few times per year (Ducrocq et al., 2014). The experiment ran for 8 months, from March 21st to October 10th in 2014. During this period, it collected data for about 170 days. There were about 25 days of rain, from which 5 could be considered heavy rain.

The geometry and measurements used for this experiment are closely related to those of the polarimetric weather radar observations. In the radar observations, the differential reflectivity ( $Z_{dr}$ ) and the specific differential phase ( $K_{dp}$ ) are the most important polarization signatures for rain characterization at low elevation angles (e.g. Bringi and Chandrasekar, 2001). Some differences apply in this case: we are limited to one single observable, the differential phase between the H- and V-ports phase delay ( $\Delta\Phi$ ), defined as:

$$\Delta\Phi = \int_L K_{dp} dl \quad (1)$$

where L is the path length under the influence of  $K_{dp}$ . The  $K_{dp}$  can be understood as a measure of the bi-refraction induced by hydrometeors that have an asymmetry between the horizontal and vertical



axis and therefore a different effective propagation constant along them. Note also that  $K_{dp}$  is here defined in propagation (forward-scattering) rather than back-scattering. This is a one dimensional observation, since it is an integral along the ray path. Furthermore, the weather radars work with frequencies equal or higher than 3 GHz, thus the sensitivity to hydrometeors is expected to be higher than for the L-band signals.

From the polarimetric radar observations it is known that different kinds of rain, precipitation and particles could produce different  $K_{dp}$ . Studies for rain (e.g. Bringi and Chandrasekar, 2001; Trömel et al., 2013), ice (e.g. Vivekanandan et al., 1994; Ryzhkov and Zrnčić, 1998), snow (e.g. Matrosov, 1992; Kennedy and Rutledge, 2011) and melting layer (e.g. Baldini and Gorgucci, 2006; Trömel et al., 2013) characterization using polarimetric observables have been widely conducted, as well as the continuous satellite observation of rain such as the Tropical Rainfall Measurement Mission (TRMM) and the Global Precipitation Mission (GPM) missions. Therefore, the aim here is not to characterize the different kinds of precipitation or hydrometeors, but to take advantage of this knowledge to understand the observations.

This paper is organized in the following way: in section 2 the experiment geometry and the acquired data are described in detail, and a comparison with the satellite set-up is performed. Problems with the signal, local multipath characterisation, and expected improvements from satellite observations are addressed here. The collocated meteorological data used for validation are described in section 3. The statistical results of the experiment are shown in section 4, and a comparison with the forward model simulation results is performed in section 5. Finally, in section 6 the conclusions are discussed.

## 2 Polarimetric GNSS data

### 2.1 Observables

GNSS signal observables are the carrier phase and the pseudorange. In the standard RO, these are measured with a circular co-polar antenna (right-handed, transmitted signals), and they are used to obtain the bending angle, which in turn is used to obtain the refractivity, pressure and temperature profiles (Kursinski et al., 1997). We refer to these as the standard RO thermodynamic profiles. The geometry found in the experiment is not a common RO configuration. Instead, the receiver is inside the atmosphere, i. e. on the ground, and therefore the tangent point - LEO trajectory is missing (see Fig.2). The lack of symmetry and the non-existence of negative elevation observations does not allow us to retrieve the standard thermodynamic profiles (Healy et al., 2002), which are going to be retrieved from the satellite in the future experiment.

Also, the fact that the receiver is on the ground means that the radio-link is crossing all the atmosphere layers during all the observation time. In this configuration, the sounding of the atmosphere is different from a RO one. This has an important implication in the observables.

The polarimetric GNSS observable  $\Delta\Phi$  is the difference between the the carrier phase delay measured in the Horizontal (H) port and and the one measured in the Vertical (V) port. The observations in the H and V ports of the polarimetric antenna are independent, and therefore the receiver treats them separately. The GNSS receivers keep track of the total phase relative to their initial measurement, but the value associated with the first measurement is arbitrary (Blewitt, 1989). In this case, both signals (H and V) suffer from this ambiguity (phase ambiguity,  $b$ ) in their respective channel:

$$\begin{aligned}\Phi_i(t) = & \rho(t) + \rho_{atm}(t) + \rho_{hyd}^i(t) + \rho_{ion}(t) \\ & + m^i(t) + d^i + C(t) + b^i\end{aligned}\quad (2)$$

where  $\Phi$  is the measured carrier phase delay at the  $i$  port (H or V).  $\rho$  is the geometry range between the satellite and the receiver since the initial measurement (the same for H and V),  $\rho_{atm}$  denotes the delay due to the neutral atmosphere that is equal in the H and V channels,  $\rho_{hyd}$  is the phase delay due to the interaction with hydrometeors (the terms that we are interested in) and  $\rho_{ion}$  denote the ionospheric delay.  $m$  represents the local multipath in each component, the term  $d$  refers to the hardware effects of the receiver and the transmitter (such as noise, the effect of a possible difference in the cable's length, etc.) and  $C$  represents the clock drifts and errors. the arbitrary initial constant that does not depend on time. Most of these terms are common in both components, thus the phase difference is:

$$\Delta\Phi(t) = \rho_{hyd}^H(t) - \rho_{hyd}^V(t) + m + b + d \quad (3)$$

where  $m = m^H - m^V$ ,  $b = b^H - b^V$  and  $d = d^H - d^V$ .

We do not have sufficiently precise pseudorange measurements to solve the initial phase bias as it is done in Blewitt (1989). The expected phase difference  $\Delta\Phi$  is in the range of  $mm$  while the pseudorange accuracies are of the order of  $cm$ . This term  $b$  changes in every arc of data (continuous tracking) and therefore the observation is not absolute, but relative to the first measurement.

To avoid further problems, we identify the breaks in the tracking of the same PRN, and we separate them in continuous arcs. Every time that the track is lost, the receiver starts again with a new arbitrary constant. For each day, we only consider the longest arc, and discard the rest. To enable comparison among different observations, we force each arc to have a 0 mean:

$$\Delta\Phi'(t) = \Delta\Phi(t) - \langle \Delta\Phi(t) \rangle. \quad (4)$$

This step homogenizes all the observations allowing the comparison among them. It removes the contribution from  $b$  and  $d$  terms, but it also erases any constant signature of the polarimetric measurement. Thus, any rain contribution in which depolarization is present since the beginning and remains until the end of the observation will be missed. In a satellite to satellite geometry (PAZ scenario), even without knowing the arbitrary initial constants we expect to be able to calibrate the initial phase, since in the beginning of the occultation the radio-link between the GPS and the LEO



130 is not crossing the atmosphere. A summary of the expected differences between the spaceborne mission and this ground experiment can be found in Table 1.

## 2.2 Local Multipath

Local multipath is the result of the combination of the signal from the satellite and one or more signals from the same source that have followed different paths to reach the receiver, for example, 135 being reflected on the ground or on a metallic structure. It affects the phase differently in the H and in the V components, giving a pattern that depends on the surrounding geometry, environmental conditions and position of the transmitter. The antenna is placed over a shelter, which has several metallic pieces. Also, there is a meteorological station a few meters from the experiment. Thus, the data suffer from a severe local multipath. If the reflecting process affected equally both H and V, this 140 effect would cancel in  $\Delta\Phi$ . However, metallic structures with longitudinal edges might differently affect the scattering in the two polarizations.

The GPS satellites have an orbit period of one sidereal day. This implies that, in ideal conditions, the local multipath pattern ought to repeat after a sidereal day since the satellite is again in the same position with respect the observation site (it follows the same azimuth - elevation curve every 145 sidereal day). To characterize and, to a large extent, remove the local multipath pattern from the signal, the time series of observations  $\Delta\Phi_{day}^{PRN}(t)$  are converted into elevation series  $\Delta\Phi_{day}^{PRN}(\epsilon)$ . Time can be mapped into elevation using the GPS orbit information, that provides a precise GPS position for each time. This conversion allows the direct comparison among the observations from different days, making the signal only dependent on the satellite position.

150 Once the direct comparison is possible, the local multipath pattern can be found performing the average and the standard deviation of the  $\Delta\Phi_{dd}^{PRN}(\epsilon)$  for a given set of days. To account for all the environmental conditions in exception for rain, the local multipath pattern is obtained using all the days identified as *no-rain* days. This identification is done taking into account information from two different sources: the ground weather station placed next to the observation site, and the radar 155 reflectivity ( $Z_e$ ) from the weather radar of the area. If the ground weather station indicates that no rain was accumulated during the observation time, and the weather radar indicates that no valid  $Z_e$  values were present between the antenna and the GPS, the day is labelled as *no-rain*. More details about the meteorological information used in the data analysis can be found in Sect. 3.

The average ( $m$ ) and the standard deviation ( $\sigma$ ) of the *no-rain* days ( $m_{no-rain}^{PRN}, \sigma_{no-rain}^{PRN}$ ) represent the local multipath pattern for *no-rain* days and can be seen in Fig. 3 top. Note that the multipath pattern features vary between GPS transmitters, because of different geometry, thus interaction with the nearby structures. Usually,  $\sigma_{no-rain}^{PRN}$  is large at low elevations. This is due to a lower quality of the signal, that has travelled a longer time through the atmosphere layers than those rays at higher elevations. To obtain the final measurement, i.e. the one that will be analysed, this local multipath

165 pattern is removed from the measured signal  $\Delta\Phi'(\epsilon)$ :

$$\Delta\Phi_{day}^{PRN}(\epsilon)|_{corrected} = \Delta\Phi_{day}^{PRN}(\epsilon)|_{measured} - m_{no-rain}^{PRN}(\epsilon). \quad (5)$$

The antenna pattern is also affecting the measurements differently in each component and induces a phase difference due to its different response to each polarization. Since the antenna is the PAZ's engineering model, the characteristics should be the same as the one mounted in the satellite and its pattern is characterized in Cardellach et al. (2015). Its effect, though, is implicitly taken into account in the  $m_{no-rain}^{PRN}$  term (it is constant in time and only depends on the satellite position), and therefore it is implicitly corrected applying Eq. 5. Hereafter, the corrected measurement will be referred to as  $\Delta\Phi_{day}^{PRN}(\epsilon)$ . An example of corrected  $\Delta\Phi_{day}^{PRN}$  is given in Fig. 3 bottom.

### 2.3 Ionosphere

175 It is well known that the ionosphere affects the GPS signal carrier phase delays and pseudorange. In terms of polarization, there are two effects that have an effect on the signals, the Faraday rotation and the Cotton-Mouton effect. The Faraday rotation is due to the longitudinal component of the Earth's magnetic field (longitudinal here meaning along the signal propagation direction), while the Cotton-Mouton effect is due to its transverse component (perpendicular to the propagation direction).

180 Faraday rotation changes the polarization axis of the propagating signals, proportionally to the total electron content (TEC) crossed and the longitudinal component of the Earth magnetic field. If the signal is transmitted at pure right hand circular polarization (RHCP) then the rotation angle effect is the same in both components, H and V, and therefore it should not be noticeable when differentiating both signals.

185 On the other hand, the Cotton-Mouton effect could induce different phase delays in each component. According to Yeh et al. (1999), under the Earth's ionospheric conditions and frequency bands higher than 25 MHz, the Cotton-Mouton effect becomes significant only when the magnetic field is almost perpendicular to the propagation (see Figures 4a and 5a, for 25MHz and 1MHz in the aforementioned reference). Otherwise, only the longitudinal (Faraday rotation) is relevant. For example, despite the magnetic field being  $\sim 80$  deg. from the propagation, the Cotton-Mouton effect is still negligible.

Given the geometry of the GPS orbits, the experimental site location and antenna boresight orientation, these conditions (B at ionospheric altitudes perpendicular to GPS signal propagation) did not happen. Note that even for a LEO in polar orbit (such as PAZ polarimetric-RO experiment will be) the probability to find B perpendicular to the propagation direction is small.

### 2.4 Measurement precision

Even though the carrier phase measurement precision could be determined as in Cardellach et al. (2015), this would not be an actual value for the real precision of the polarimetric phase shift mea-

200 surement in this experiment. Many factors, such as multipath, add dispersion to the observations and affect the actual precision of the measurement. These effects cannot be theoretically characterized and removed, but they have to be empirically determined.

Besides multipath, other effects are, for instance, a non-perfectly circular polarization of the emitted signals, which could lead to small polarimetric ionospheric effects (the waves emitted by the GPS satellites are in principle perfectly RHCP, but they admit a small tolerance). Also temperature variations in the surrounding media could change the dielectric constant of the media, and therefore slightly modify the multipath pattern day after day. Among others, these effects add dispersion to the polarimetric phase shift measurement and cannot be disentangled among them. Therefore, they end up included in the  $\sigma_{no-rain}^{PRN}$  term in Eq. 5.

### 3 Meteorological weather data

210 The objective of the analysis is to understand the new polarimetric observations, which requires collocated meteorological information. The weather radar of the area, in-situ radiosonde data and METEOSAT satellites measurements near the GNSS observational site are used in this study.

The Servei Meteorològic de Catalunya (METEOCAT) has a weather radar network covering the Catalan coastal area (Bech et al., 2004). We have access to the data from one of the radars, which has full coverage of the area under study. These radars are all Doppler systems, with one single polarization, operating at C-band (5.6 GHz). The provided data consists of the radar reflectivity ( $Z_e$ ) in  $dBZ$ , as a function of latitude, longitude and height. Its resolution is  $1 \times 1 \times 1 km$  in a grid of  $300 \times 300 km$ , per  $10 km$  of height, and every 6 minutes. Since it is not a polarimetric radar, we can not extract information such as  $K_{dp}$  or  $Z_{dr}$ , which would provide clues about the orientation of the particles. The minimum  $Z_e$  value that is considered valid is  $0 dBZ$ , below that the signal is considered noise and it is removed.

METEOCAT also has a network of ground stations that provides the accumulated precipitation, temperature and relative humidity in 30 minutes batches. In a radius of 30 km around the observation site, there are 5 ground weather stations, with one locating a few meters from the GNSS antennas. Through them we can have an approximation of the surface rain rate during the rain events.

Besides the radar and ground stations data, Cloud Type (CTY), Cloud top Phase (CP) and Cloud Top Height (CTH) data products from the Nowcasting and Very Short Range Forecasting (NWC-SAF) have been used. The data have been provided by the Agencia Estatal de Meteorología (AEMET) and the European Organisation for the Exploitation of Meteorological Satellites (EUMETSAT). These data products are a combination of satellite observations and Numerical Weather Prediction (NWP) model simulations. The satellite observations are obtained by the MSG stationary meteorological satellites. They measure brightness temperatures and radiances with a radiometer at 12 different wavelengths (4 ranging from  $0.4$  to  $1.6 \mu m$  and 8 ranging from  $3.9$  to  $13.4 \mu m$ ). The

horizontal resolution is  $\sim 3$  km and the products are available for the study area every 15 minutes  
235 (Aminou, 2002).

Th collocated cloud observations from NWC-SAF (CTY, CP and CTH) are then interpolated  
with the GNSS ray trajectories. Unfortunately, the points of data do not provide information about  
the orientation of the ice particles. Only those with its major axis oriented horizontally would induce  
a positive polarimetric signature. These data is mainly used to identify the top of the clouds, and to  
240 identify ice above the maximum radar products height.

To complement all the information we use the measurements provided by METEOCAT's ra-  
diosondes. These radiosondes are launched two times per day (00 and 12 UTC) at a distance of  
approximately 50 km to the South-East of the antenna, and provide temperature, pressure and hu-  
midity as a function of height. With the limited two-time daily soundings, the temperature and re-  
245 fractivity profiles can be interpolated into the GNSS observation time.

Once all the information is recompiled, we can perform exact collocations of the GNSS polari-  
metric observations with the weather data. To do so, we first simulate the rays from the GPS to the  
antenna using a ray-tracer called OAT, which solves the trajectory of each ray across the atmosphere  
characterized by the retrieved refractivity profiles (Aparicio and Rius, 2004). An illustration of the  
250 performed collocation can be seen in Fig. 4. Then, we interpolate all the weather information for  
each of the points of the ray trajectory. For this analysis, each ray consists of 500 points, separated  
 $\sim 0.52$  km among them. We simulate 501 rays, between 0 and 20 degrees of elevation.

## 4 Statistical results: Do rain induce polarimetric features?

### 4.1 Polarimetric signatures in $\Delta\Phi$ standard deviations

255 Once the data have been pre-processed as described in Sect. 2, the analysis should determine whether  
the corrected  $\Delta\Phi_{day}^{PRN}(\epsilon)$  is affected by rain or not. To do so, corrected  $\Delta\Phi_{day}^{PRN}$  are grouped accord-  
ing to three different meteorological conditions. For each group, the standard deviation as a function  
of elevation  $\sigma_{met}^{PRN}(\epsilon)$  is computed. The three meteorological conditions and the corresponding  $\sigma$   
are:

- 260 – Dry days: days when the observation was made in a low relative humidity conditions (i.e. the  
relative humidity has not reached 100%) according to the nearby weather ground station, and  
without rain ( $\sigma_{dry}^{PRN}(\epsilon)$ ). No rain is stated when the nearby weather ground stations do not  
accumulate any rain during the observation time and the interpolation of the weather radar  
data along the GNSS rays does not cross any area where valid  $Z_e$  values ( $Z_e > 0$ ) are detected.
- 265 – Wet days: days either with high relative humidity (i.e. the relative humidity has reached 100%)  
according to the nearby weather ground station during or before the observation; or rain before  
or after the observation; or both ( $\sigma_{wet}^{PRN}(\epsilon)$ ).

- Rain days: Days when the GNSS rays have crossed an area where valid  $Z_e$  values are detected by the weather radar ( $\sigma_{rain}^{PRN}(\epsilon)$ ).

270 This classification has been done in order to compare different meteorological conditions. For example, high relative humidity conditions could have caused condensation, leading to a wet soil and different local multipath and antenna behaviour. The mean  $\sigma$  across all elevation observations for each GNSS satellite during the three different meteorological conditions are summarized in Table 2.

275 It can be seen that *dry* days present always a lower  $\sigma$  in the rest, and that *rain* days exhibit the largest  $\sigma$ . The standard deviation for *wet* days is also larger than for *dry* days, but the difference is less significant than for the *rain* days. There should not be any significant differences between *wet* and *rain* days, in terms of the surroundings condition. For example, just after rain, the soil should be as wet as during rain. Therefore, the larger  $\sigma$  in *rain* days compared with the *wet* days indicates 280 other factors should have contributed to the enhanced polarimetric signature other than the enhanced local multipath due to the wet soil in the *rain* days.

To check if this difference is enough to be treated as different populations (i.e the cause of the different standard deviations is that  $\sigma$  under different scenarios and not due to a different sampling) a simple statistical test called F-test is performed (Walpole et al., 2012). We define the  $f$  statistic as 285 the ratio of the variances ( $\sigma^2$ ) of the populations we are comparing, the  $P_F$  as the cumulative probability of  $f$ , and we compare the *rain* days with the *no-rain* days, where the *no-rain* are all the *wet* and *dry* days. The results of  $P_F$  are shown in Table 2. It can be understood as the significance level that we are rejecting the null hypothesis, that in this case is that the variances that we are comparing come from the same pool. It can be seen that 4 out of the 5 analysed PRNs have a  $P_F$  large 290 enough to state that there exist a difference in the standard deviation that could be related to rain.

Hereafter and for the rest of the analysis, the correction of the  $\Delta\Phi_{day}^{PRN}(\epsilon)$  is done as described in Eq. 5 using  $m_{no-rain}^{PRN}$ , which is computed as in Sec. 2.2 accounting for all the *dry* and *wet* days defined in this section together.

#### 4.2 Phase difference as a function of elevation

295 Examining each event individually, more features can be observed. To do such analysis, we compare each observation  $\Delta\Phi_{day}^{PRN}(\epsilon)$  with the  $\sigma_{no-rain}^{PRN}(\epsilon)$ . We define a  $2\sigma_{no-rain}^{PRN}$  threshold to detect polarimetric signatures in the signal: statistically speaking,  $\sim 95\%$  of the data should be within  $\pm 2\sigma_{no-rain}^{PRN}$ . The remaining 5% of the data points and those affected by some polarimetric feature should lay beyond  $\pm 2\sigma_{no-rain}^{PRN}$ .

300 Lacking an absolute reference for the phase difference and to identify points overpassing the  $\pm 2\sigma_{no-rain}^{PRN}(\epsilon)$  threshold, we find the elevation point where the difference between  $\Delta\Phi_{day}^{PRN}(\epsilon)$  and  $-2\sigma_{no-rain}(\epsilon)$  is minimum, and we identify it as  $\epsilon_{min}$ . Then, we subtract this difference from the observation, and what is obtained is the observation aligned in a way that for each event its minimum



lays on the line of  $-2\sigma_{no-rain}$  threshold:

$$305 \quad \Delta\Phi_S(\epsilon) = \Delta\Phi(\epsilon) - (\Delta\Phi(\epsilon_{min}) + 2\sigma_{no-rain}(\epsilon_{min})) \quad (6)$$

Defining  $2\sigma_{no-rain}^{PRN}(\epsilon)$  as the no-rain noise level,  $\Delta\Phi_S$  can be understood as a bias-corrected settled phase difference. After this correction, we can easily detect the points outside the  $2\sigma$  threshold. The region of  $\Delta\Phi_S(\epsilon)$  above the  $+2\sigma_{no-rain}$  threshold is defined as follows:

$$\Delta\Phi_+(\epsilon) = \begin{cases} \Delta\Phi_S(\epsilon) - 2\sigma(\epsilon) & \text{if } \Delta\Phi_S(\epsilon) > 2\sigma(\epsilon) \\ 0 & \text{if } \Delta\Phi_S(\epsilon) \leq 2\sigma(\epsilon) \end{cases} \quad (7)$$

310  $\Delta\Phi_+(\epsilon)$  would be the phase difference above the statistical no-rain noise level and its area is defined as  $A_\Phi$ :

$$A_\Phi = \int \Delta\Phi_+(\epsilon) d\epsilon \quad (8)$$

An example of  $\Delta\Phi_S(\epsilon)$  and  $A_\Phi$  is shown in the bottom plot in Fig.5. In this procedure, we only consider the option of positive phase differences, as it is expected for rain effects (Cardellach et al., 315 2015). We have found 30 observations with  $A_\Phi > 0$ , of which 28 correspond to rainy scenarios. This is the first direct observational evidence of the polarimetric signatures induced by precipitation conditions in the GNSS signals.

## 5 Are the observed polarimetric features consistent with the models?

In order to explain the observations, forward scattering calculations have been performed. The aim 320 is to simulate the effect of several kinds of hydrometeors, such as rain drops, pristine ice particles and melting ice particles, to cross-compare with weather radar reflectivities, satellite observations and the phase differences measured.

First of all, the  $K_{dp}$  and the radar reflectivity factor ( $Z_e$ ) have been calculated for each hydrometeor type. These calculations have been done using the DDScat code (Draine and Flatau, 1994, 325 2013).

DDScat provides the phase lag efficiency factor ( $Q_{pha}$ ) for each polarimetric component H and V. It is related to the forward scattering amplitude  $f_{sca}$  through  $Q_{pha} = \frac{2\pi}{k} \frac{\Re\{f_{sca}\}}{\pi a_{eff}^2}$ . Thus, it can be used to calculate the  $K_{dp}$ :

$$K_{dp} = \frac{\lambda}{2\pi} \int (Q_{pha}^H - Q_{pha}^V) \pi a_{eff}^2 N(D) dD \quad (9)$$

330 where  $a_{eff}$  is the equivolumetric radius of the particle,  $N(D)$  is the particle size distribution,  $D$  is the equivolumetric diameter and  $K_{dp}$  is in  $mm/km$ .

DDScat also provides the differential backscattering cross section normalized by  $\pi a_{eff}^2$ :

$$Q_{bk} = \frac{1}{\pi a_{eff}^2} \left. \frac{\partial \sigma_{sca}}{\partial \Omega} \right|_{\Theta=180} \quad (10)$$

The backscattering cross section can then be obtained:

$$335 \quad \sigma_{bk} = 4\pi Q_{bk} \pi a_{eff}^2 \quad (11)$$

Using the  $\sigma_{bk}$ , the radar reflectivity factor  $Z_e$  can be calculated as follows:

$$Z_e = \frac{\lambda^4}{\pi^5 |K_w|^2} \int_0^{D_{max}} \sigma_{bk}(D) N(D) dD \quad (12)$$

where  $\lambda$  is the wavelength,  $K_w = (m_w^2 - 1)/(m_w^2 + 2)$  and  $m_w$  is the complex refractive index of water (Smith, 1984).

340  $K_{dp}$  is calculated for L-band frequency (GNSS observations), and  $Z_e$  for C-band frequency (weather radar observations). This will allow to relate the reflectivity from the weather radar in C-band with the GNSS observations in L-band.

The  $N(D)$  that has been used is a gamma function of the form:

$$N(D) = N_0 D^\mu e^{-\Lambda D} \quad (13)$$

345 where  $N_0$  is the scale parameter,  $\Lambda$  is the slope parameter and  $\mu$  is the shape parameter (Ulbrich, 1983). These are the 3 parameters of the gamma  $N(D)$ . The particle size distribution can be used to determine other quantities such as the  $K_{dp}$  (e.g. Eq.9),  $Z_e$  (e.g. Eq.12), liquid or ice water content ( $LWC$ ,  $IWC$ ), effective particle diameter ( $D_{eff}$ ), mean weighted diameter ( $D_m$ ) and rain rate ( $R$ ). Further details of the relation between these magnitudes and the  $N(D)$  can be found in the literature, 350 for example in Williams et al. (2014).

Since there is not a unique parameterization of the  $N(D)$  that apply to all scenarios, we generate a set of mathematically valid  $(N_0, \Lambda, \mu)^i$  triplets, each one producing a different  $N(D)^i$ . Then, each triplet has an associated physical magnitude:

$$(N_0, \Lambda, \mu)^i \rightarrow N(D)^i \rightarrow (K_{dp}^i, Z_e^i, LWC^i, D_{eff}^i, D_m^i, R^i, \dots)$$

Depending on the hydrometeor being modelled, not all  $N(D)$  parameters will be physically consistent, that is, fall in ranges that have been observed amongst various ground validation data (Williams et al., 2014). In the next section we describe the selection criteria for the valid ranges to choose among the possible  $N(D)^i$ .

### 355 5.1 Modelled $A_\Phi$ : rain effects



At the beginning of the campaign, only rain was expected to affect the polarimetric signal. To simulate the polarimetric rain effect, the  $Q_{pha}$  and  $\sigma_{bk}$  have been calculated with DDScat using the predetermined oblate spheroid shapes, with  $D$  ranging from 0.1 to 6 mm, and AR following the Beard and Chuang (BC) relation (Beard and Chuang, 1987), as it was done in Cardellach 360 et al. (2015). Shape is sketched in Fig 6 (left). Some constraints have been applied to the  $(N_0, \Lambda, \mu)$

triplets in order to use only those producing physically valid quantities: we have limited  $R$  to be as high as  $70 \text{ mm/h}$  as suggested by the meteorological ground stations, and an upper limit of  $LWC$  is set to be  $3 \text{ g/m}^3$  according to the observational evidence of severe storms described in Black and Hallett (2012). All the parameter triplets producing quantities out of these ranges are discarded.

365 From the chosen  $N(D)$  we derive  $Z_e$  and  $K_{dp}$ . All the valid  $Z_e^i$  and  $K_{dp}^i$  for rain conditions are shown in black in Fig. 7. To relate the observations from the weather radar and the measurements from the polarimetric antenna, we need to use a  $Z_e - K_{dp}$  relation. It can be seen in Fig. 7 how a wide range of possible  $K_{dp}$  can be related to a given  $Z_e$ . For simplicity, we will use the  $Z_e - K_{dp}$  indicated with a thick line in Fig. 7.

370 We have simulated the expected  $A_\Phi$  caused by rain for every GNSS measurements, using the radar  $Z_e$  values interpolated to GNSS ray trajectories, and this  $Z_e - K_{dp}$  relation. The results can be seen in black dots in Fig. 8. Despite the polarimetric signatures happening on rainy days, Fig. 8 shows that rain drops alone do not induce the large polarimetric signals observed (black dots in Fig. 8). Therefore, the effects of other hydrometeors must be taken into account.

## 375 5.2 Could ice and melting particles explain the large polarimetric signatures?

We aim here to simulate the expected  $A_\Phi$  induced by icy and melting particles. To simulate the ice particles, dendritic shapes have been used. Their characteristics are described in Liu (2008). For melting ice particles, two concentric ellipsoids have been used: the inner one made of pristine ice and the outer one of water. Both have the same axis ratio, ranging from 0  0.8, and with  $D$  ranging from 0.01 to  $6 \text{ mm}$ . The water shell is considered to range between a 5 and a 10 % of the volume of the inner core. Their shapes are sketched in Fig 6  (center and right).

A given ice-induced  $Z_e$  can be explained by a diversity of ice particle characterizations, such as different combinations of canting angle,  $IWC$ , percentage of horizontally oriented particles with respect to randomly oriented ones, or predominant sizes of the particles, among others. This diversity of ice conditions relate to a diversity of  $K_{dp}$ . This means that a given  $Z_e$  links to many possible  $K_{dp}$  values. Since we want to keep this modelling simplistic to understand the contributions and an order of magnitude of the polarimetric effect, and because we do not have ancillary information to properly characterize the ice properties, we have simulated this effect using only horizontally oriented dendrites, with a maximum  $IWC$  of  $1 \text{ g/m}^3$ . Horizontal orientation is supported by many studies, for example Matrosov and Mace (2012) or Noel and Chepfer (2010). The  $IWC$  maximum is chosen accordingly to the maximum values observed in Delanoë and Hogan (2010). The chosen  $Z_e^i$  and  $K_{dp}^i$  for ice particles are shown in Fig. 7 in blue, and the  $Z_e - K_{dp}$  relation used for ice particles is highlighted with a thick blue line.

395 Melting ice particles have even a wider range of variability. As can be seen in Fig. 7 (in gray), the possible  $Z_e^i$  and  $K_{dp}^i$  are widely spread. We have used the  $Z_e - K_{dp}$  relation indicated with a gray thick line when accounting for melting ice particles. As for rain and pristine ice, this relation is rather



arbitrary, as we do not have the required ancillary ground-truth information to properly characterize these particles, and the goal is to explain, to an order of magnitude, the measurements.

We have separated the contribution of rain, ice, and melting ice particles according to the temperature. The temperatures are given by the METEOCAT's radiosondes, mentioned in Sect. 3. Noting that the radiosonde observation may differ in exact location and time, these are the closest to a true value of the temperature profiles. These radiosonde observations are on the GPS antenna field of view. For the cells above land (like the ones analysed here), METEOCAT profiles are less than 50 km away and temperatures above the boundary layer should be representative. The radar reflectivity measured at heights with temperatures above  $1^{\circ}\text{C}$  is considered to come from rain. Particles in the range between  $1^{\circ}\text{C}$  and  $-5^{\circ}\text{C}$  are assumed to be melting ice particles. Below  $-5^{\circ}\text{C}$  they are assumed to be ice. Ice particles are assumed to be bigger in the range between  $-5$  and  $-20^{\circ}\text{C}$ , because this region is considered to be the maximum dendritic growth zone (Kennedy and Rutledge, 2011). Above the radar measurements, ice contributions are assumed when the simulated ray intersects with ice regions, according to the combination of the Cloud top Phase and Cloud Top Height products from the NWC-SAF. In this case, the particles are assumed to be smaller. We assume a thickness of the ice particle layer of about 2 km, in agreement with Noel and Chepfer (2010).

In addition, the contribution to  $A_{\Phi}$  due to ice and melting particles is only simulated when the observed  $\Delta\Phi_{+}(\epsilon)$  is positive. The reason is that if there were no measurement of  $\Delta\Phi_{+}(\epsilon)$ , there would not be oriented crystals in the ray path, nor a contribution to  $K_{dp}$ . The Cloud-Aerosol Lidar and Infrared Pathfinder Satellite Observations (CALIPSO) images show how only some regions of the clouds contain oriented ice crystals. This is consistent with discontinuous positive observations of  $\Delta\Phi$ , as is observed here. Unfortunately, no collocations were found between CALIPSO and the experiment.

The results for the simulated  $A_{\Phi}$  taking into account the different hydrometeors are shown in orange dots in Fig. 8. For every black dot (only rain simulated) an orange dot is included. Since they try to reproduce the same observed  $A_{\Phi}$ , there will be a black and an orange dot for every observed  $A_{\Phi}$ . A block diagram is shown in Fig. 9 to help the reader follow the steps that lead to the Fig. 8 results. All the data, information and relations used from the data acquisition to the final results are summarized in it.

Comparing the corresponding black and orange dots for a given observed  $A_{\Phi}$ , one can notice how the simulated  $A_{\Phi}$  increases significantly using all three hydrometeor types with respect to using only rain. Also, in most of the cases the simulated  $A_{\Phi}$  is larger than the measured one (see the slope of the best fitted lines, dot-dashed in Fig. 8). This means that we tend to overestimate  $A_{\Phi}$  in the simulations. Indeed, the particle characteristics that we have used in the simulations may increase the  $K_{dp}$ : the orientation of the particles is assumed to be horizontal (maximizing the polarimetric effect), and the type of particles is taken to be very asymmetric (when reality is more diverse).

Moreover, the model has been applied using the same  $Z_e - K_{dp}$  relation for each hydrometeor type, in every analysed rainy event. Fine tuning of the parameters for each individual observation would be needed in order to fairly reproduce the observations, but this would not be possible to validate due to the lack of ancillary independent information, and it is thus beyond the scope of this work. Yet, it can be seen how the inclusion of icy and melting particles besides rain can explain the order of magnitude of the observations.

### 5.3 Illustration cases

In order to further check the internal consistency of the measurements, a comparison among several observations for different PRN is performed, during the evolution of heavy rain episodes. In this section we analyse three of such episodes: events on 2014/06/14, 2014/08/22 and 2014/05/26. To do so, we show the weather radar data, the observed phase difference above the noise level ( $\Delta\Phi_+$ ) and the simulated  $\Delta\Phi_+$ . An example can be seen in Fig. 10. It corresponds to PRN 22 on 2104/06/14.

The figure shows each GNSS ray identified by its elevation angle. Every point along the ray is associated with its height (left Y axis) and it is coloured according to the corresponding radar reflectivity  $Z_e$  (from the interpolation between the GNSS rays and the weather radar). Besides that, every elevation angle is associated to a  $\Delta\Phi_+$  measurement (it is an along-ray integral measurement) and it is plotted as a thick black line that is ruled by the right Y axis. The simulated  $\Delta\Phi_+$  is plotted with dashed lines along with the measured  $\Delta\Phi_+$ , and is also ruled by the right Y axis. Therefore, in these figures it can be shown the measured phase difference plotted overlaying the radar reflectivity that is inducing it, and a comparison with the results of the simulation. A temporal series of such plots along heavy rain episodes are shown in Figures 11 and 12.

Figure 11 corresponds to events on 2014/06/14, 2014/08/22 and 2014/05/26, (same day represented in the same column) respectively:

- In the case of 2014/06/14, according to the nearby meteorological ground stations, there were maximum accumulations of rain of 14 mm in 30 minutes. This corresponds to peaks of rain rate higher than 28 mm/h. Large positive  $\Delta\Phi$  is present when large radar reflectivity ( $Z_e$ ) is accumulated at high altitudes. This is in agreement with the fact that rain alone produces lower polarimetric signatures than the ones detected with the present configuration.
- On 2014/08/22, the nearby meteorological ground stations suggest peaks of rain rate higher than 55 mm/h according to the accumulated precipitation over 30 minutes. As in the previous case, positive  $\Delta\Phi$  measurements are observed in the regions where significant  $Z_e$  reaches high altitudes, and where the temperature is around or below  $0^\circ C$  (ice and melting particles).
- The last case, on 2014/05/26, there were not such high rain rate peaks, but significant  $Z_e$  is also present at high altitudes, in agreement with the positive  $\Delta\Phi$  observations.

Among all the studied cases (30), more than 93% (28) can be explained with the combined hydrometeor modelling, i.e. the modelling can reproduce the order of magnitude of the observations. An example of one of the two cases in which the simulations failed to explain the observations can be seen in Fig. 12, on 2014/07/09. In this case, positive  $\Delta\Phi$  measurements can not be associated with any significant radar reflectivity, nor to ice in the tops of the clouds crossed by the ray. Possible explanations could be some discrepancies due to missing observational data in the radar, or errors in the temperature (that relies in the radiosonde interpolation) that might lead to a bad hydrometeor identification.

## 475 6 Conclusions

For the first time, GNSS occulting signals have been acquired using a two-polarization antenna and the evidence of the polarimetric signature induced by hydrometeors in the GNSS signals has been presented. The technique, presented in Cardellach et al. (2015), will be tested from space aboard the PAZ Low Earth Orbiter. If successful, it will be possible to provide rain flags, and potentially information about rain structures, collocated with the standard RO thermodynamic profiles.

The experiment presented here was intended to characterize the phenomena that are actually affecting the polarimetric signatures. It has consisted of comparing the measurements of the polarimetric observable  $\Delta\Phi$  under different weather conditions, trying to identify rain signatures. Data from 5 GNSS transmitters on  $\sim 170$  different days have been analysed.

485 Many challenges have arisen in the data analysis process. Three main issues affect the data: the location of the antenna/receiver (low inside the atmosphere, not proper RO geometry), the phase ambiguity problem (linked to internal processing of the commercial receiver), and severe and varying local multipath (mostly due to the nearby environment, metallic towers and structures). These effects are not expected (or milder) in the spaceborne mission: Regarding the location of the antenna/receiver, the future experiment will be in the space, and therefore outside the atmosphere. Being outside the atmosphere will allow a better calibration of the signals thanks to the scanning geometry: a vertical descent from the outer layers approaching the Earth surface. Thus, at the beginning of the observation there are no depolarizing effects, and it will be possible to define the initial state (calibration of the polarimetric phase measurement). Phase ambiguity will be solved, and absolute measurements will be possible, unlike in this experiment. Also, in the satellite we expect the local multipath to be smaller, and most importantly, it will not change with the environmental conditions.

490 After analysing the data, two main conclusions can be extracted. In a general view, rain scenarios affect the polarimetric observables. The standard deviation of the mean  $\Delta\Phi$  for *dry*, *wet* and *rain* days have been examined. For environmental reasons (wet soil, increase of the reflectivity, etc.), the  $\sigma$  for *wet* and *rain* days is higher than for *dry* days. However, the increase of the  $\sigma_{rain}$  with respect  $\sigma_{dry}$  is between 20 and the 40% larger than the increase of  $\sigma_{wet}$  with respect  $\sigma_{dry}$ .

This could empirically answer one of the questions that we were seeking for an answer: Are radio-links crossing rain cells affected by any depolarization affect? And if so, is it detectable? According to the  $\sigma$  behaviour under the different weather and environmental conditions, we can answer that  
505 under rain scenarios, the measured  $\Delta\Phi$  suffer from higher variability, and the difference from other scenarios is noticeable.

A more detailed analysis of the  $\Delta\Phi(\epsilon)$  has been performed for each individual observation.  $\Delta\Phi$  above the defined  $2\sigma$  threshold, and the computed  $A_\Phi$  have been compared with simulated results. Simulated  $K_{dp}$  using the collocated radar reflectivity has shown that rain drops induce an effect  
510 much lower than the measurements. This indicates that other phenomena are inducing polarimetric signatures too. This is an important point in views to the future analysis of the spaceborne ROHP-PAZ data.

Ice crystals and melting ice particles have been added to the modelling, using temperature information and satellite imagery to distinguish between hydrometeors. Simulations of these particles  
515 have been kept very simplistic, due to the number of possible parameters involved in the modelling and the lack of information to validate them. The goal at this stage is to identify the sources of polarimetric signatures. The simulations have shown that, in most of the cases, the measured  $\Delta\Phi$  could be explained by the  $K_{dp}$  induced by all possible hydrometeors.

Simulated  $\Delta\Phi$  and  $A_\Phi$  with all the hydrometeors are usually above the measured values. Fine  
520 tuning of the parameter involved in the modelling would be needed in order to match the observations, but nevertheless impossible to validate in this particular experiment. Microphysical analysis of the precipitation and inversion procedures development are left for later studies with RO, data more suitable than mountain-top occultations. Yet, the results obtained here represent the first empirical  
525 evidence that hydrometeors induce measurable polarimetric signatures in occulting GNSS signals after the theoretical analysis in Cardellach et al. (2015). These results are helping us to understand the types of processes affecting the data from the future polarimetric RO experiment aboard PAZ. They additionally show the potential capability of polarimetric RO to sense complex precipitable structures, information that will be provided along with thermodynamic profiles and increase the applications of the RO technique.

530 *Acknowledgements.* This study has been conducted under the Spanish ACI2010-1089 and AYA2011-29183-C02-02 grant, with contributions from EUMETSAT's ROM SAF CDOP2 and two NASA ROSES. RP is under the Spanish FPI program and he also enjoyed two JPL Vistor Student Researcher Program invitations. EC is under the Spanish Ramon y Cajal programme. A relevant contribution to the logistics and implementation of the experimental site was done by Adriano Camps' group at the Remote Sensing Lab, department of Teoria del Senyal i Comunicacions, Universitat Politècnica de Catalunya, under grant AYA2011-29183-C02-01.  
535 Some of these grants are partially funded by the European ERDF/FEDER programme. Work performed at the Jet Propulsion Laboratory (JPL), California Institute of Technology, was supported under a contract with the National Aeronautics and Space Administration.

The Helmholtz-Centre German Research Centre for Geosciences (GFZ Potsdam) provided the JAVAD GPS  
540 receiver. Results obtained thanks to the meteorological data provided by the Servei Meteorològic de Catalunya  
(METEOCAT), the Agencia Estatal de Meteorología, Ministerio de Agricultura, Alimentación y Medio Ambiente (AEMET) and the European Organisation for the Exploitation of Meteorological Satellites (EUMETSAT).  
The experimental site belongs to the Spanish Ministry of Defense, Estado Mayor de la Defensa (EMAD).

Bruce T. Draine and Piotr J. Flatau are gratefully acknowledged for providing the DDscat code. Particle  
545 shapes for DDScat code were provided by Dr. G. Liu and Ryan Honeyager, from Florida State University. The  
authors want to thank G. Hajj for interesting discussions about the ionosphere.

## References

- Aminou, D. M.: MSG's SEVIRI Instrument, *ESA Bulletin*, 111, 15–17, 2002.
- Aparicio, J. M. and Rius, A.: A raytracing inversion procedure for the extraction of the atmospheric refractivity from GNSS travel-time data, *Physics and Chemistry of the Earth, Parts A/B/C*, 29, 213–224, doi:10.1016/j.pce.2004.01.008, <http://linkinghub.elsevier.com/retrieve/pii/S1474706504000191>, 2004.
- 550 Baldini, L. and Gorgucci, E.: Identification of the melting layer through dual-polarization radar measurements at vertical incidence, *Journal of Atmospheric and Oceanic Technology*, 23, 829–839, doi:10.1175/JTECH1884.1, 2006.
- 555 Beard, K. V. and Chuang, C.: A new model for the equilibrium shape of raindrops, *Journal of the Atmospheric sciences*, 44, 1509–1524, [http://journals.ametsoc.org/doi/abs/10.1175/1520-0469\(1987\)044%3C1509:ANMFTE%3E2.0.CO;2](http://journals.ametsoc.org/doi/abs/10.1175/1520-0469(1987)044%3C1509:ANMFTE%3E2.0.CO;2), 1987.
- Bech, J., Vilaclara, E., Pineda, N., Rigo, T., Lopez, J., O'Hora, F., Lorente, J., Sempere, D., and Fabregas, F. X.: The weather radar network of the Catalan Meteorological Service: description and applications, in: Proceedings of ERAD, vol. 2, pp. 416–420, 2004.
- 560 Black, R. A. and Hallett, J.: Rain Rate and Water Content in Hurricanes Compared with Summer Rain in Miami, Florida, *Journal of Applied Meteorology and Climatology*, 51, 2218–2235, doi:10.1175/JAMC-D-11-0144.1, <http://journals.ametsoc.org/doi/abs/10.1175/JAMC-D-11-0144.1>, 2012.
- Blewitt, G.: Carrier phase ambiguity resolution for the Global Positioning System applied to geodetic baselines up to 2000 km, *Journal of Geophysical Research*, 94, 10 187–10 203, doi:10.1029/JB094iB08p10187, 1989.
- 565 Brangi, V. N. and Chandrasekar, V.: *Polarimetric weather radar; principles and applications*, Cambridge University Press, 2001.
- Cardellach, E., Tomás, S., Oliveras, S., Padullés, R., Rius, A., de la Torre-Juárez, M., Turk, F. J., Ao, C. O., Kursinski, E. R., Schreiner, W., Ector, D., and Cucurull, L.: Sensitivity of PAZ LEO Polarimetric GNSS Radio-Occultation Experiment to Precipitation Events, *IEEE Transactions on Geoscience and Remote Sensing*, 53, 190–206, doi:10.1109/TGRS.2014.2320309, 2015.
- 570 Cucurull, L. and Derber, J. C.: Operational Implementation of COSMIC Observations into NCEP's Global Data Assimilation System, *Weather and Forecasting*, 23, 702–711, doi:10.1175/2008WAF2007070.1, <http://journals.ametsoc.org/doi/abs/10.1175/2008WAF2007070.1>, 2008.
- 575 Delanoë, J. and Hogan, R. J.: Combined CloudSat-CALIPSO-MODIS retrievals of the properties of ice clouds, *Journal of Geophysical Research*, 115, D00H29, doi:10.1029/2009JD012346, <http://doi.wiley.com/10.1029/2009JD012346>, 2010.
- Draine, B. T. and Flatau, P. J.: Discrete-dipole approximation for scattering calculations, *Journal of the Optical Society of America A*, 11, 1491, doi:10.1364/JOSAA.11.001491, <http://www.opticsinfobase.org/abstract.cfm?URI=josaa-11-4-1491>, 1994.
- 580 Draine, B. T. and Flatau, P. J.: User Guide for the Discrete Dipole Approximation Code DDSCAT 7.3, arXiv preprint, 3, <http://arxiv.org/abs/1305.6497>, 2013.
- Ducrocq, V., Braud, I., Davolio, S., Ferretti, R., Flamant, C., Jansa, A., Kalthoff, N., Richard, E., Taupier-Letage, I., Ayrat, P. A., Belamari, S., Berne, A., Borga, M., Boudevillain, B., Bock, O., Boichard, J. L., Bouin, M. N., Bousquet, O., Bouvier, C., Chiggiato, J., Cimini, D., Corsmeier, U., Coppola, L., Cocquerez, P., Defer, E., Delanoë, J., Di Girolamo, P., Doerenbecher, A., Drobinski, P., Dufournet, Y., Fourrié, N., Gourley,

- J. J., Labatut, L., Lambert, D., Le Coz, J., Marzano, F. S., Molinié, G., Montani, A., Nord, G., Nuret, M., Ramage, K., Rison, B., Roussot, O., Said, F., Schwarzenboeck, A., Testor, P., Van Baelen, J., Vincendon, B., Aran, M., and Tamayo, J.: HyMeX-SOP1, the field campaign dedicated to heavy precipitation and flash  
590 flooding in the northwestern Mediterranean, *Bulletin of the American Meteorological Society*, 95, 1083–1100, doi:10.1175/BAMS-D-12-00244.1, <http://journals.ametsoc.org/doi/abs/10.1175/BAMS-D-12-00244.1?af=R>, 2014.
- Healy, S. B., Haase, J. S., and Lesne, O.: Abel transform inversion of radio occultation measurements made with a receiver inside the Earth's atmosphere, *Annales Geophysicae*, 20, 1253–1256, 2002.
- 595 Healy, S. B., Jupp, A. M., and Marquardt, C.: Forecast impact experiment with GPS radio occultation measurements, *Geophysical Research Letters*, 32, L03 804, doi:10.1029/2004GL020806, <http://doi.wiley.com/10.1029/2004GL020806>, 2005.
- Kennedy, P. C. and Rutledge, S. A.: S-Band Dual-Polarization Radar Observations of Winter Storms, *Journal of Applied Meteorology and Climatology*, 50, 844–858, doi:10.1175/2010JAMC2558.1, <http://journals.ametsoc.org/doi/abs/10.1175/2010JAMC2558.1>, 2011.  
600
- Kursinski, E. R., Hajj, G. A., Schofield, J. T., Linfield, R. P., and Hardy, K. R.: Observing Earth's atmosphere with radio occultation measurements using the Global Positioning System, *Journal of Geophysical Research*, 102, 23 429–23 465, doi:10.1029/97JD01569, <http://onlinelibrary.wiley.com/doi/10.1029/97JD01569/full>, 1997.
- 605 Liu, G.: A Database of Microwave Single-Scattering Properties for Nonspherical Ice Particles, *Bulletin of the American Meteorological Society*, 89, 1563–1570, doi:10.1175/2008BAMS2486.1, <http://journals.ametsoc.org/doi/abs/10.1175/2008BAMS2486.1>, 2008.
- Matrosov, S. Y.: Radar reflectivity in snowfall, *IEEE Transactions on Geoscience and Remote Sensing*, 30, 454–461, doi:10.1109/36.142923, 1992.
- 610 Matrosov, S. Y. and Mace, G. G.: Observations of ice crystal habits with a scanning polarimetric W-band radar at slant linear depolarization ratio mode, *Journal of Atmospheric and Oceanic Technology*, 29, 989–1008, doi:10.1175/JTECH-D-11-00131.1, <http://journals.ametsoc.org/doi/abs/10.1175/JTECH-D-11-00131.1>, 2012.
- Noel, V. and Chepfer, H.: A global view of horizontally oriented crystals in ice clouds from Cloud-Aerosol  
615 Lidar and Infrared Pathfinder Satellite Observation (CALIPSO), *Journal of Geophysical Research*, 115, doi:10.1029/2009JD012365, <http://doi.wiley.com/10.1029/2009JD012365>, 2010.
- Rocken, C., Anthes, R. A., Exner, M., Hunt, D., Sokolovskiy, R., Ware, R. H., Gorbunov, M., Schreiner, W., Feng, D., Herman, B. M., Kuo, Y. H., and Zou, X.: Analysis and validation of GPS/MET data in the neutral atmosphere, *Journal of Geophysical Research*, 102, 29,849–29,866, doi:10.1029/97JD02400,  
620 <http://onlinelibrary.wiley.com/doi/10.1029/97JD02400/full>, 1997.
- Ryzhkov, A. V. and Zrnić, D. S.: Polarimetric method for ice water content determination, *Journal of Applied meteorology*, 37, 125–134, [http://ieeexplore.ieee.org/xpls/abs/\\_all.jsp?arnumber=516402](http://ieeexplore.ieee.org/xpls/abs/_all.jsp?arnumber=516402), 1998.
- Smith, P. L.: Equivalent Radar Reflectivity Factors for Snow and Ice Particles, *Journal of Climate and Applied Meteorology*, 23, 1258–1260, doi:10.1175/1520-0450(1984)023<1258:ERRFFS>2.0.CO;2, 1984.

- 625 Steiner, A. K., Lackner, B. C., Ladstetter, F., Scherllin-Pirscher, B., Foelsche, U., and Kirchengast,  
G.: GPS radio occultation for climate monitoring and change detection, *Radio Science*, 46, 1–17,  
doi:10.1029/2010RS004614, 2011.
- Trömel, S., Kumjian, M. R., Ryzhkov, A. V., Simmer, C., and Diederich, M.: Backscatter differen-  
tial phase-estimation and variability, *Journal of Applied Meteorology and Climatology*, 52, 2529–2548,  
630 doi:10.1175/JAMC-D-13-0124.1, 2013.
- Ulbrich, C. W.: Natural Variations in the Analytical Form of the Raindrop Size Distribution, *Journal of Climate*  
and *Applied Meteorology*, 22, 1764–1775, doi:10.1175/1520-0450(1983)022<1764:NVITAF>2.0.CO;2,  
1983.
- Vivekanandan, J., Bringi, V. N., Hagen, M., and Meischner, P.: Polarimetric radar studies of atmospheric ice  
635 particles, *IEEE Transactions on Geoscience and Remote Sensing*, 32, 1–10, doi:10.1109/36.285183, [http:  
//ieeexplore.ieee.org/lpdocs/epic03/wrapper.htm?arnumber=285183](http://ieeexplore.ieee.org/lpdocs/epic03/wrapper.htm?arnumber=285183), 1994.
- Walpole, R. E., Myers, R. H., Myers, S. L., and Ye, K.: *Probability and Statistics for Engineers and Scientists*,  
Prentice Hall, Boston, 9th edn., 2012.
- Williams, C. R., Bringi, V. N., Carey, L. D., Chandrasekar, V., Gatlin, P. N., Haddad, Z. S., Meneghini, R.,  
640 Joseph M., S., Nesbitt, S. W., Petersen, W. A., Tanelli, S., Tokay, A., Wilson, A., and Wolff, D. B.: Describing  
the Shape of Raindrop Size Distributions Using Uncorrelated Raindrop Mass Spectrum Parameters, *Journal*  
*of Applied Meteorology and Climatology*, 53, 1282–1296, doi:10.1175/JAMC-D-13-076.1, [http://journals.  
ametsoc.org/doi/abs/10.1175/JAMC-D-13-076.1](http://journals.ametsoc.org/doi/abs/10.1175/JAMC-D-13-076.1), 2014.
- Yeh, K. C., Chao, H. Y., and Lin, K. H.: A study of the generalized Faraday effect in several media, *Radio*  
645 *Science*, 34, 139–153, doi:10.1029/98RS02442, <http://doi.wiley.com/10.1029/98RS02442>, 1999.



**Table 1.** Summary of the relevant differences expected between the ROHP-PAZ spaceborne experiment and the conducted ground-based field campaign.

| Parameter              | Ground-based experiment   | ROHP-PAZ   |
|------------------------|---|--|
| Initial phase delay    | unknown, need to subtract the mean value of each measured arc (Eq. 4)   | calibrated from the polarimetric phase difference at highest layers of the atmosphere              |
| Local multipath        | multiple reflectors and environmental dependency because of dry/wet changes in electrical permittivity of soil and structures | expected stable properties of local satellite structure. No expected dependency on the environment |
| Thermodynamic profiles | refractivity, pressure, temperature and humidity cannot be extracted  | refractivity, pressure, temperature and humidity can be derived                                    |

**Table 2.** Summary of the standard deviation analysis for the polarimetric phase differences under three different meteorological conditions (dry, wet and rain days).  $\bar{\sigma}_i$  and  $N_i$  account for the mean standard deviation and the number of used days for each meteorological condition group  $i$ .  $P_F$  is the cumulative probability associated to the  $f$  statistic comparing the  $\sigma$  of the rain and the no-rain (wet and dry) days. The  $f$  statistic is the result of the F-test and  $P_F$  can be understood as the significance level at which we are rejecting the null hypothesis that both populations come from the same pool.

| $PRN$ | $\bar{\sigma}_{dry}$ (mm) | $N_{dry}$ | $\bar{\sigma}_{wet}$ (mm) | $N_{wet}$ | $\bar{\sigma}_{rain}$ (mm) | $N_{rain}$ | $P_F$ |
|-------|---------------------------|-----------|---------------------------|-----------|----------------------------|------------|-------|
| G10   | 2.706                     | 20        | 2.895                     | 112       | 3.992                      | 25         | 0.99  |
| G15   | 1.808                     | 20        | 2.263                     | 108       | 2.597                      | 29         | 0.89  |
| G22   | 2.565                     | 20        | 3.167                     | 113       | 3.738                      | 24         | 0.91  |
| G14   | 3.386                     | 20        | 3.698                     | 114       | 4.108                      | 23         | 0.79  |
| G31   | 1.809                     | 20        | 1.876                     | 113       | 2.584                      | 24         | 0.99  |

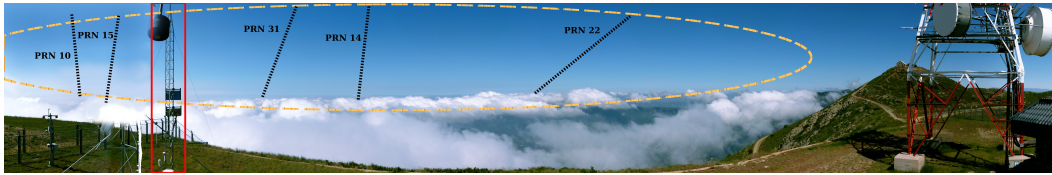


**Figure 1.** Panoramic view from the observation site. The field of view is the area compressing azimuths from  $\sim 160^\circ$  (left) to  $\sim 270^\circ$  (right), looking south. The yellow long-dashed line indicates the main lobe of the antenna (approximate). The black dashed lines represent the tracks of the followed GPS satellites: from left to right, PRN 10, 15, 31, 14 and 22. Multiple metallic elements seen in the field of view, such as the meteorological station (inside the red solid line square), the fence, the telecommunications antenna, etc. and others not pictured (metallic shelter, antenna supports...) could affect the GNSS signal in the form of multipath.

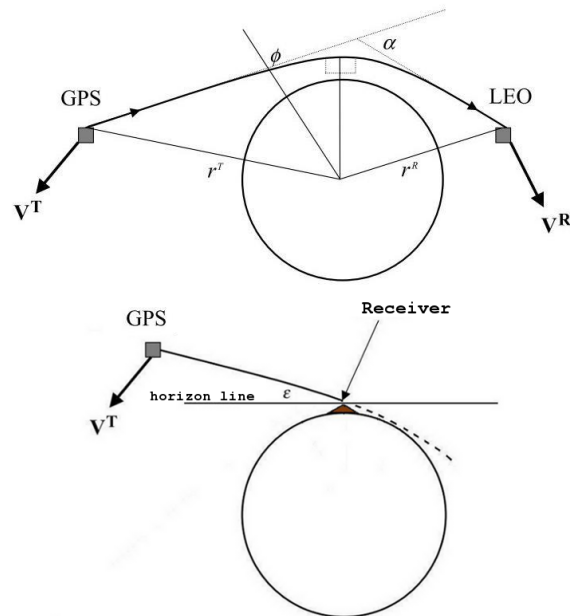


**Figure 2.** (top) Standard radio occultation geometry. (bottom) GPS-receiver radio link in a on ground receiver geometry, such as the one used in this experiment.  $\epsilon$  accounts for elevation. Edited figure from original in Healy et al. (2002).

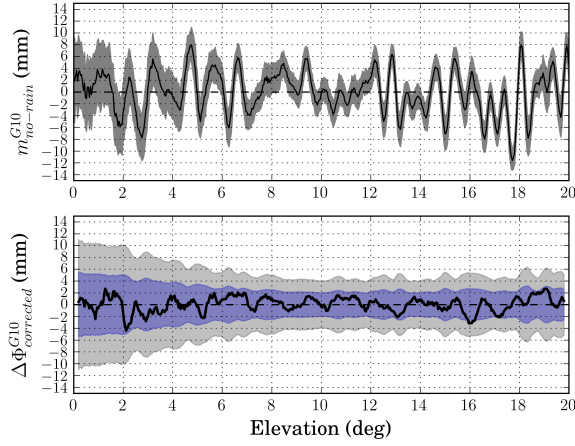


**Figure 3.** Examples of (top) local multipath pattern after Eq. 4 for PRN 10 ( $m_{no-rain}^{G10}, \sigma_{no-rain}^{G10}$ ), using a total of 132 days defined as *no-rain* days. Notice the large standard deviation at lower elevations, and  $\sigma_{no-rain}^{G10}$  of about 2 mm at higher elevations. (bottom) Corrected  $\Delta\Phi_{day}^{PRN}(\epsilon)$  for 2014/04/16 (black line) after applying Eq. 5. The 1- and 2- $\sigma$  thresholds (local multipath standard deviation) are represented in blue and gray, respectively.

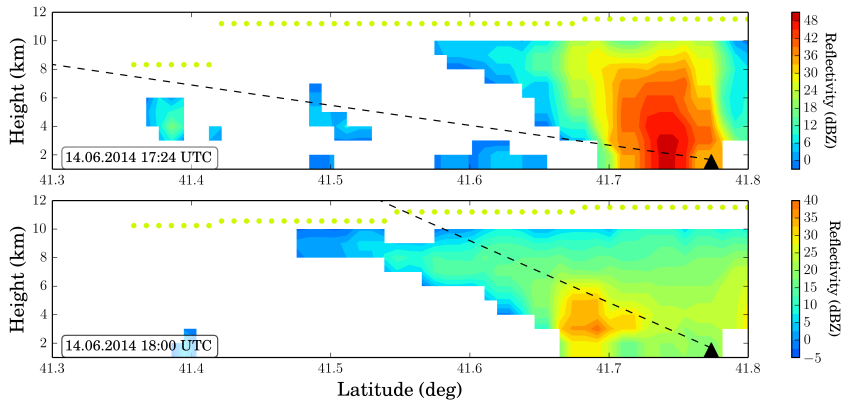


**Figure 4.** A vertical slice of radar reflectivity (shaded) at two epochs of a rising GNSS occultation event. The dashed black line is the projection of the ray trajectory as simulated with OAT ray tracer on the described plane, and the dots correspond to the Cloud top Phase (CP) products. In this case, all the green dots indicate ice in the top of the clouds.

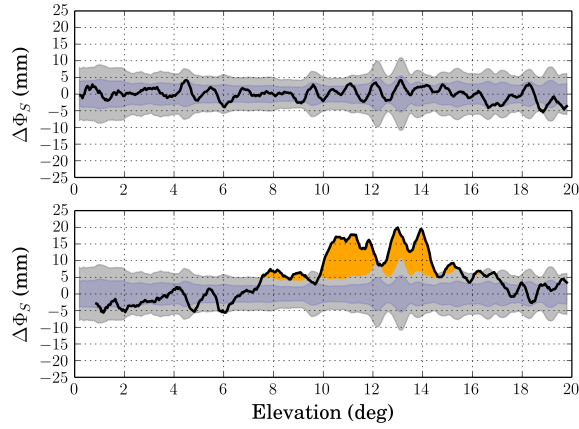


**Figure 5.** Examples of  $\Delta\Phi_S(\epsilon)$  (black line), the  $\pm\sigma_{no-rain}$  contour (blue) and the  $\pm 2\sigma_{no-rain}$  contour (gray), for two observations of the *PRN* G22 during 2014/05/26 (top) and 2014/06/14 (bottom). The top  $\Delta\Phi_S(\epsilon)$  measurement is well inside the  $2\sigma$  contour, showing no polarimetric signatures. On the bottom, case on 2014/06/14 shows large positive  $\Delta\Phi_S(\epsilon)$ . The value of  $\Delta\Phi_S(\epsilon)$  above  $2\sigma_{no-rain}$  threshold will be called hereafter  $\Delta\Phi_+$ , and its area (orange zone)  $A_\Phi$ .

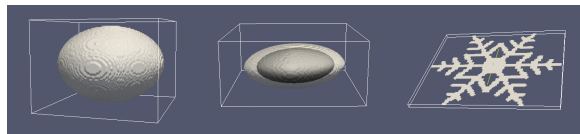


**Figure 6.** Particle shape models used in DDScat. (left) Oblate ellipsoid for rain drops, (middle) two concentric ellipsoids for melting ice particles, with an ice core and a water shell, (right) dendritic shape for pristine ice particles.

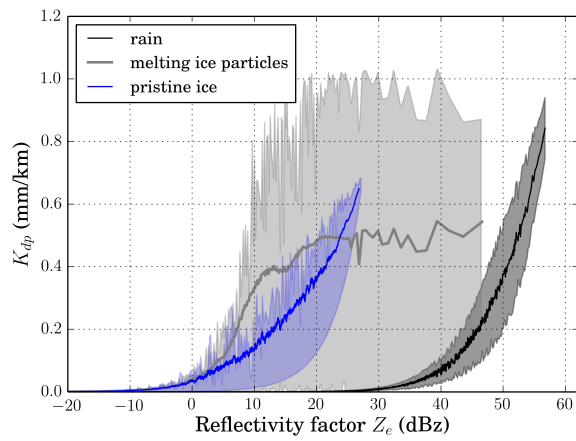


**Figure 7.**  $K_{dp}(Z_e)$  for all the possible physically valid  $N(D)$  for each hydrometeor type: rain (black), melting ice particles (gray) and ice crystals (blue). Rain drops need high reflectivity to produce high  $K_{dp}$ , while ice crystals and melting ice particles can induce high values of  $K_{dp}$  at smaller values of  $Z_e$ . The thick lines overlotted represent the  $Z_e - K_{dp}$  relation used in this analysis for each hydrometeor type.

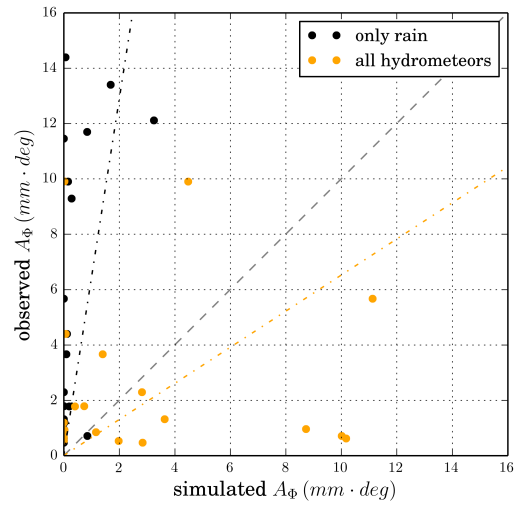
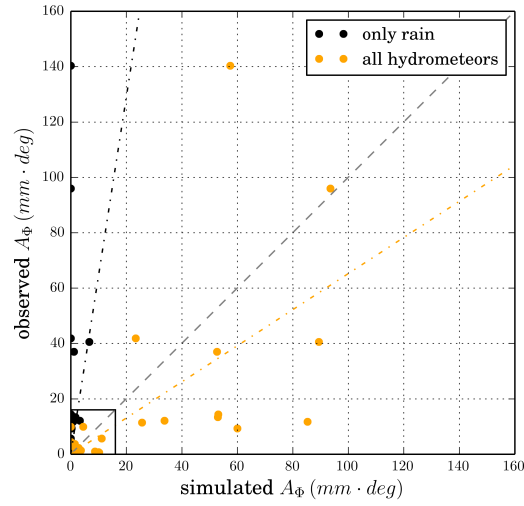


**Figure 8.** (top) Observed versus simulated  $A_\Phi$ . (bottom) In more detail, the area where  $A_\Phi < 20$  mm-deg. Black dots represent the simulated  $A_\Phi$  using only rain drops, while orange dots represent the simulated  $A_\Phi$  accounting for ice crystals and melting ice particles too. The dash-dot lines represent the best fitted line to the only rain  $A_\Phi$  (black) and to the rain, ice and melting particles  $A_\Phi$  (orange).

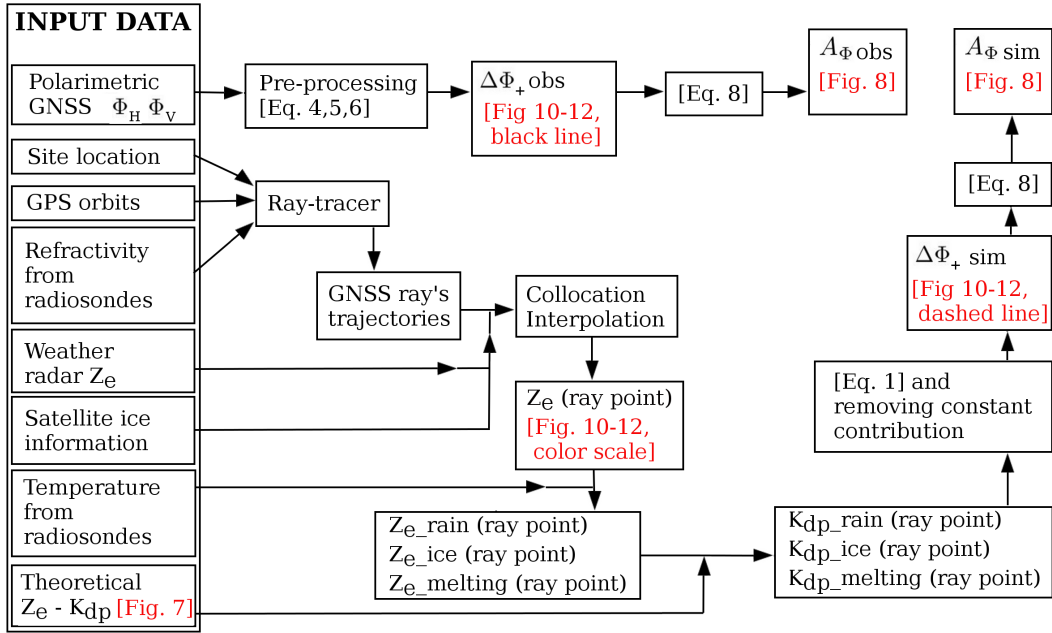


**Figure 9.** Block diagram showing all the data analysis and modelling process. Steps from the data acquisition to the final results are shown.

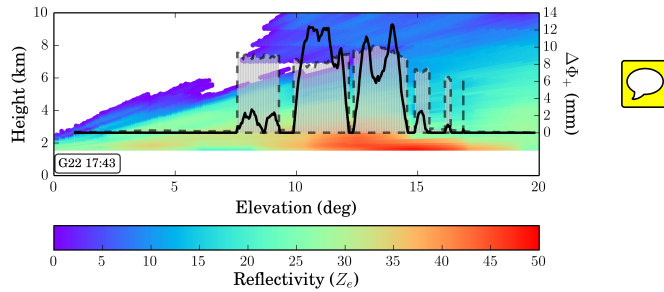


**Figure 10.** Each GNSS ray is identified by its elevation angle. Along a ray, each point can be identified by its height. The color scale shows the weather radar reflectivity  $Z_e$  interpolated along the GNSS rays. The black line is the observed  $\Delta\Phi_+$  (right Y axis). Simulation results performed as described in Sect. 5 are represented with dashed lines. In the regions where actual data showed  $\Delta\Phi_+ > 0$ , all hydrometeors are taken into account in the simulations. Only rain is simulated otherwise. Note also that fully oriented ice crystals have been considered in the simulation (it might not be necessary the case, information not available).

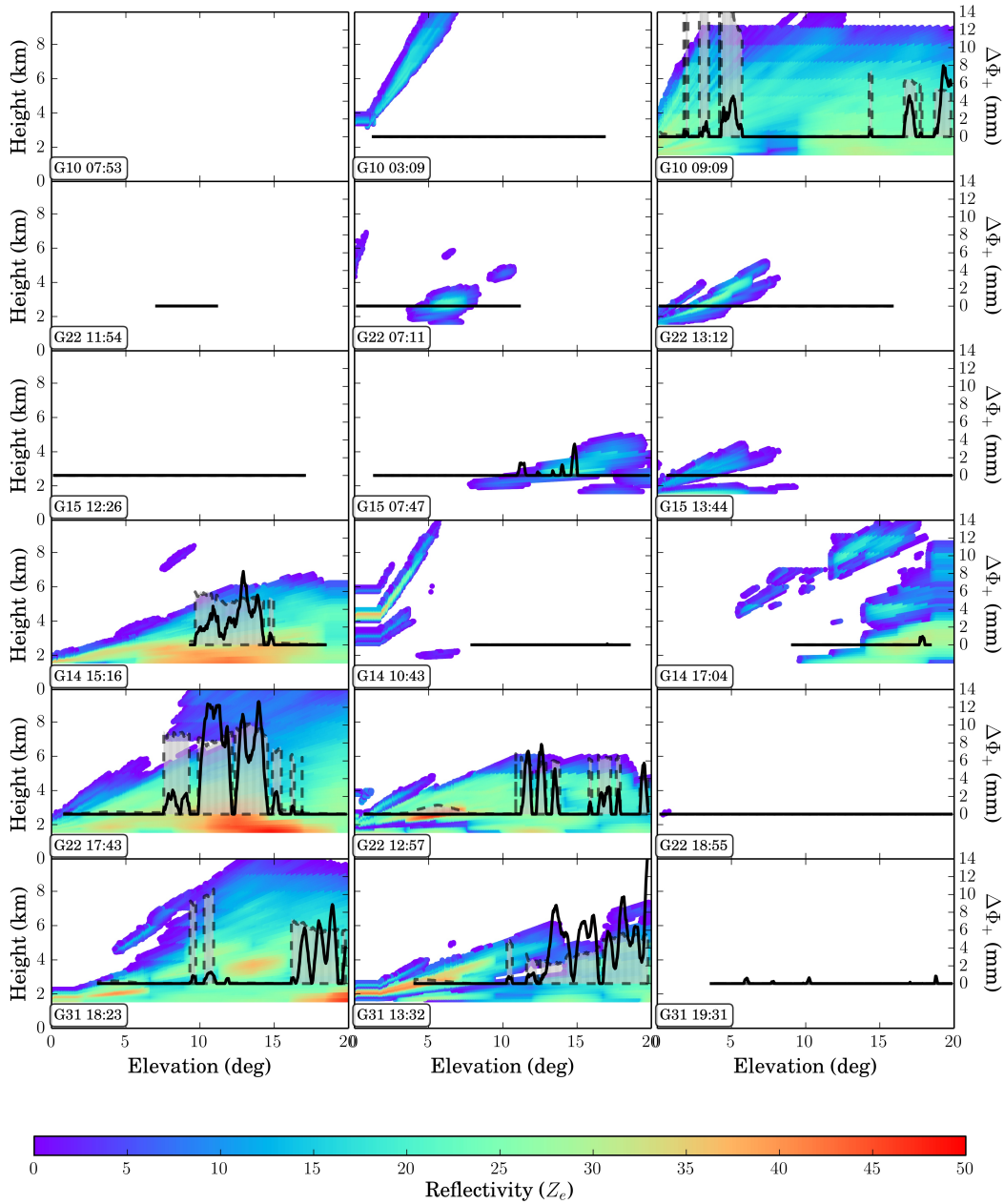


**Figure 11.** Rain episodes on 2014/06/14 (left), 2014/08/22 (middle) and 2014/05/26 (right). Each panel corresponds to a PRN, identified in the label on the lower left corner, along with the time when the satellite is at 10 deg. of elevation. Note that the radio-link with different PRNs corresponds to different time and also different azimuth. They are sorted in time, with the first one on the top. Content of each panel is explained in [Fig. 10 caption](#).



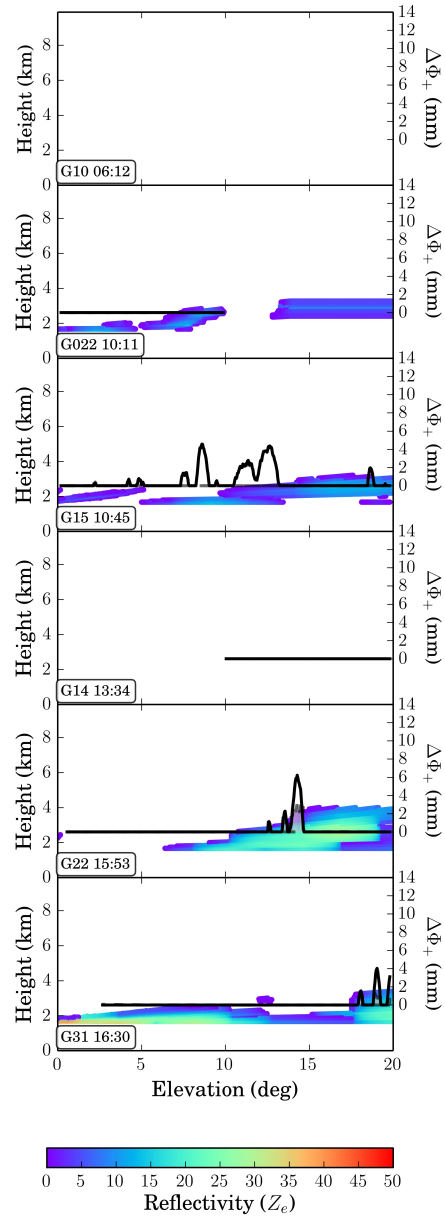


**Figure 12.** Same as Fig.11, but for 2014/07/09. The signal in PRN G15 could not be explained with the model simulation.